Geochemical Perspectives Letters

Kinetics of low-temperature H_2 production in ultramafic rocks by ferroan brucite oxidation

W. Carlin, B. Malvoisin, F. Brunet, B. Lanson, N. Findling, M. Lanson, T. Fargetton, L. Jeannin, O. Lhote

Supplementary Information

The Supplementary Information includes:

- Characterisation Techniques
- Time Needed to Reach Thermodynamic Equilibrium in Titanium Reactors
- H_2 Production Rate-law
- Retrieval of $\Delta_f H°$ and $S°$ of the $Fe(OH)_2$ End Member: Calculation Method
- Numerical Modelling of H_2 Production During Serpentinised Dunite Alteration
- Tables S-1 to S-4
- Figures S-1 and S-4
- Supplementary Information References

An overview of the notation used throughout is given in Table S-1.

Characterisation Techniques

Gas phase contained in the sealed gold capsules was recovered after the experiments using the method described in Malvoisin *et al.* (2013). For titanium reactors, the gas phase was sampled in a syringe connected to the reactor headspace through a valve. For the gas analysis, 250 µL of gas was injected with gas-tight syringe in a Clarus 500 gas chromatograph (Perkin Elmer™) equipped with a polymer filled column (Restek ShinCarbon™) and a thermal conductivity detector (TCD). Argon was used as carrier gas. Each gas sample was analysed at least three times to check reproducibility. Based on these repeated measurements, the uncertainty on H_2 measurement is estimated to be ~11 % of the measured values (one standard deviation).

The recovered sample powder was characterised by X-ray diffraction (XRD) with a Bruker D8 diffractometer. XRD patterns were collected from 10 to 80° (2θ) using CuKα or CoKα radiation and counting times of 3 s per 0.04° step (Fig. S-1). XRD patterns were analysed using the Rietveld technique with the BGMN software (Doebelin and Kleeberg, 2015). Details of both the refinement strategy and refinement constraints are given in Carlin *et al.* (2023). The results of gas analyses and Rietveld refinement are provided in Tables S-2 and S-3.

Sample powders were mounted on double-sided carbon tape in the glove box for scanning electron microscopy (SEM) imaging. They were then coated under vacuum with a 1 nm thick gold layer and characterised with a field emission gun scanning electron microscope (FEG-SEM; Zeiss Ultra 55) operated at 5 to 10 kV.

Time Needed to Reach Thermodynamic Equilibrium in Titanium Reactors

Pressure evolution in SP experiments was monitored *in situ* (Fig. S-2). The hydrogen partial pressure, P_{H_2}, and thus the amount of produced H_2, n_{H_2}, were not retrieved from the *in situ* pressure monitoring. Indeed, as illustrated in Figure S-2, a steady state regime is achieved after an initial step of pressure increase but the steady-state pressure cannot be precisely retrieved due to a noise amplitude of ~30 kPa in the measured pressure. These variations have actually the same amplitude as the pressure increase generated by the reaction itself. For example, in experiment SP#5, the pressure oscillation (0.41–0.37 MPa) is equal to 40 kPa, *i.e.* close to the pressure increase generated by the complete reaction (Fig. S-2).

The *in situ* pressure monitoring could however be used to constrain the kinetics of ferroan brucite oxidation by retrieving the approximate reaction time needed to reach steady-state pressure conditions, even though the exact steady-state pressure could not be accurately determined. Steady-state pressure was assumed to represent near equilibrium conditions, and the corresponding reaction time was determined graphically for each SP experiments (Fig. S-2).

H_2 Production Rate-law

In the experiments conducted in gold capsules at ~20 MPa, no gas phase is present and H_2 occurs as an aqueous phase only:

$$3[Fe(OH)_2]^{brucite} = Fe_3O_4 + H_{2,aq} + 2H_2O. \qquad \text{(S-1)}$$

In the other experiments conducted on the liquid/vapour equilibrium, H_2 can be present as a gas phase:

$$3[Fe(OH)_2]^{brucite} = Fe_3O_4 + H_{2,g} + 2H_2O. \qquad \text{(S-2)}$$

We assumed in the following that the kinetics of Reactions S-1 and S-2 are the same. This implies that H_2 transfer between the aqueous and the gaseous phases is not a rate-limiting step (*i.e.* rapid compared to the other processes involved in the reaction). Under this assumption, hydrogen production rate (r) according to Reactions S-1 and S-2 can be written, following Lasaga (1998), as:

$$r(t) = \frac{d\bar{n}_{H_2}}{dt} = r_0 \times (1 - \frac{Q_i}{K_i}), \qquad \text{(S-3)}$$

with $r_0 = k_0 \times A \times \exp(\frac{-E_a}{RT})$. Q_i is computed by assuming that H_2 is an ideal gas and that the activity of $Fe(OH)_2$ in ferroan brucite is equal to its molar fraction ($X_{Fe(OH)_2}$). This leads for Reaction S-1 to $Q_1 = \frac{[H_{2,aq}]}{X_{Fe(OH)_2}^{\ 3}}$ with $[H_{2,aq}] = \frac{n_{H_2}}{V_{aq}}$, and for Reaction S-2 to $Q_2 = \frac{P_{H_2}}{X_{Fe(OH)_2}^{\ 3}}$ with $P_{H_2} = \frac{n_{H_{2,g}} \times R \times T}{V_g}$. Introducing

Henry's coefficient ($K_H = \frac{P_{H_2}}{[H_2]}$) allows to relate $n_{H_2,g}$ to n_{H_2} as $n_{H_2,g} = \frac{K_H V_g}{K_H V_g + RT V_{aq}} n_{H_2}$. Assuming that V_{aq} and V_g remain constant during the experiment provides the same expression for $\frac{Q_r}{K_r}$ in Reactions S-1 and S-2:

$$\frac{Q_1}{K_1} = \frac{Q_2}{K_2} = \frac{n_{H_2}}{n_{H_2,eq}} \left(\frac{X_{Fe(OH)_2,eq}}{X_{Fe(OH)_2}} \right)^3. \quad \text{(S-4)}$$

Combining Equation S-4 with an expression of $X_{Fe(OH)_2}$ derived from mass conservation in Reactions S-1 and S-2 ($X_{Fe(OH)_2} = \frac{n^\circ Fe - 3n_{H_2}}{n^\circ Fe - 3n_{H_2} + n^\circ Mg}$) allows to express $r(t)$ as a function of n_{H_2} only as:

$$r(t) = \frac{d\bar{n}_{H_2}}{dt} = \frac{r_0}{f(n_{H_2}(t))}, \quad \text{(S-5)}$$

where $f(n_{H_2}(t)) = \frac{1}{1 - \frac{n_{H_2}(t)}{n_{H_2,eq}} \times \left(\frac{(n^\circ Fe - 3n_{H_2,eq})(n^\circ Fe - 3n_{H_2}(t) + n^\circ Mg)}{(n^\circ Fe - 3n_{H_2,eq} + n^\circ Mg)(n^\circ Fe - 3n_{H_2}(t))} \right)^3}$.

We measured n_{H_2} by sampling the gas phase either at the end of the experiment (298 K) or *in situ* (experiment SP#6). During all these measurements, the calculated fraction of H_2 in the aqueous phase is below 3 mol % and was thus neglected. The value of n_{H_2} at equilibrium ($n_{H_2,eq}$) was set to the last measurement of H_2 times a factor (λ) slightly above 1 to account for the fact that n_{H_2} asymptotically tends towards the value at the equilibrium according to Reaction S-3. λ was varied between 1.01 and 1.2 to estimate its impact on the derived kinetic constants (Fig. 2). The parameter r_0 was determined by least-square regression of Equation S-5 through the experimental n_{H_2} dataset. The activation energy and the $k_0 \times A$ product were retrieved with a linear fit in a $\ln(r_0)$ *vs.* $1/T$ plot.

Retrieval of $\Delta_f H°$ and $S°$ of the $Fe(OH)_2$ End Member: Calculation Method

For Reactions S-1 and S-2 with H_2 in either the aqueous or gas phase, by definition:

$$\Delta_r G^{P,T} = \left(\sum_i^{\text{phases}} \nu_i \, \Delta_a H_i^{P,T} \right) - T \times \left(\sum_i^{\text{phases}} \nu_i \, S_i^{P,T} \right) + RT \ln \prod_i a_i{}^{\nu_i}, \quad \text{(S-6)}$$

with $\Delta_a H_i^{P,T} = \Delta_f H_i^\circ + \int_{Tr}^{T} Cp_i dT + V_i^0 (P - P_r)$ and $S_i^{P,T} = S_i^\circ + \int_{Tr}^{T} \frac{Cp_i}{T} dT$.

Equation S-6 can be simplified assuming equilibrium conditions, *i.e.* $\Delta_r G^{P,T} = 0$ and $\prod_i a_i{}^{\nu_i} = K$ and expressed as a function of two unknowns, $\Delta_f H^\circ{}_{Fe(OH)_2}$ and $S^\circ{}_{Fe(OH)_2}$. All the other parameters can be calculated from tabulated data (slop98.dat database and Klein *et al.*, 2009 for other amakinite parameters).

Considering the experimental dataset with all the experiments (j) having reached equilibrium at T_j and P_j, a system of equations is obtained:

$$\Delta_f H^\circ{}_{Fe(OH)_2} - T_j \times S^\circ{}_{Fe(OH)_2} = f_j(T_j, P_j). \quad \text{(S-7)}$$

$\Delta_f H^\circ{}_{Fe(OH)_2}$ and $S^\circ{}_{Fe(OH)_2}$ values are then determined by least-squares regression (Fig. S-3).

Numerical Modelling of H_2 Production During Serpentinised Dunite Alteration

A numerical model was developed to determine the contribution of both olivine and ferroan brucite to H_2 production during the reaction of a partly serpentinised dunite at 363 K. The initial composition of the serpentinised dunite was determined by assuming that half of the olivine was already serpentinised according to the following reaction (initial serpentinisation degree of 50 %):

$$\underset{\text{Olivine}}{24\ (Mg_{0.9}Fe_{0.1})_2SiO_4} + \underset{\text{Water}}{34\ H_2O} = \underset{\text{Serpentine}}{12\ Mg_3Si_2O_5(OH)_4} + \underset{\text{Ferroan brucite}}{9\ (Mg_{0.8}Fe_{0.2})(OH)_2} + \underset{\text{Magnetite}}{Fe_3O_4} + H_2 \qquad \text{(S-8)}$$

This leads to an initial mineral assemblage with molar fractions in ferroan brucite, olivine, serpentine and magnetite of 20 mol %, 52 mol %, 26 mol % and 2 mol %, respectively.

The production of H_2 during serpentinised dunite alteration at 363 K was considered to depend on three processes: (i) ferroan brucite alteration, (ii) olivine serpentinisation, and (iii) H_2 leakage due to fluid flow or diffusion (also referred to as 'H_2 escape rate' in the main text).

Regarding (i), ferroan brucite was considered to form magnetite according to Reaction 1 at the rate provided in Equation S-3. The value of $n_{H_2,eq}$ required in this latter equation was computed with PHREEQC considering H_2 in equilibrium with an assemblage composed of ferroan brucite + magnetite + chrysotile. The llnl.dat database was used with the thermodynamic data for ferroan brucite derived in the previous section.

Olivine serpentinisation (ii) was modelled according to Reaction S-8. The rate of H_2 production was modelled with the following surface-dependent zero-order rate law:

$$\frac{dn_{H_2,ol}}{dt} = -\left(\frac{1}{24}\right)\frac{dn_{ol}}{\partial t} = k_{ol} SAM_{ol} n_{ol}(t). \qquad \text{(S-9)}$$

M_{ol} is the molecular weight of olivine. k_{ol} is calculated as $\frac{k_{MD}}{SA_{MD}}$. One should note that, on the contrary to ferroan brucite alteration rate (Eq. S-3), $n_{H_2,ol}$ does not depend on the total amount of H_2, n_{H_2}. This is consistent with thermodynamic predictions of complete olivine reaction even at high activity in H_2 (*e.g.*, McCollom and Bach, 2009). Ferroan brucite formed during olivine serpentinisation (Reaction S-8) is also added to the amount of ferroan brucite available for H_2 production (ferroan brucite alteration (i)).

H_2 "leakage" (iii) was assumed to be proportional to the H_2 concentration in the fluid expressed as the number of moles of H_2 in the fluid over the mass of water in contact with the rock at each time step:

$$\frac{dn_{H_2,leak}}{dt} = \frac{-n_{H_2}}{m_{water}} J. \qquad \text{(S-10)}$$

J is assumed here to be constant. For the fluid flow case, J corresponds to the rate of water renewal. In this latter case, a cumulative water to rock ratio can be calculated as the integral of J over time. Moreover, fluid flow also induces Mg, Si and Fe transport as aqueous species. The solubility of Mg, Fe and Si in the fluid at the equilibrium with serpentinised dunite were retrieved from the thermodynamic calculation performed with PHREEQC in (i). The predicted pH is 9.7. The solubility in Mg of 6.2×10^{-5} mol/kg at 363 K is approximately 4 and 5 orders of magnitude higher than for Si and Fe, respectively. Ferroan brucite is thus predicted to be the main phase to dissolve during the simulation. The product of Mg solubility by the cumulative water to rock ratio was used to estimate the extent of ferroan brucite dissolution associated with fluid flow.

For the diffusion case, J can be expressed as:

$$J = \frac{D\rho_{\text{water}}A_{\text{h}}}{z}. \quad \text{(S-11)}$$

Combining Equations S-10 and S-11 and assuming $n_{H_2} = 0$ at the surface ($z = 0$) allow to retrieve Fick's first law of diffusion. A maximum of $\frac{dn_{H_2,\text{leak}}}{dt}$ for diffusion can be estimated by using $n_{H_2} = n_{H_2,\text{eq}}$, D corresponding to H_2 diffusion in bulk water (no tortuosity; 5×10^{-9} m^2/s at 298 K), z = 2500 m by using a geothermal gradient of 30 K/km, ρ_{water} = 1000 kg/m^3 and $A_{\text{h}} = \frac{m_{\text{rock}}}{\rho_{\text{rock}}h}$ with ρ_{rock} = 3000 kg/m^3 and h = 1 m, the minimum estimated thickness for reacting serpentinised peridotites at depth. With these values, the maximum diffusive flux of H_2 is of 1.3×10^{-15} mol H_2/day/g rock.

Equations S-3, S-9 and S-10 define a system of three differential equations. This system was numerically solved with an adaptive time step depending on the maximum of n_{H_2} variation for each process.

Supplementary Tables

Table S-1 Symbols used.

Symbol	Definition	Units
$X_{Fe(OH)_2}$	molar fraction of $Fe(OH)_2$ in brucite	–
$X_{Fe(OH)_2,eq}$	equilibrium molar fraction of $Fe(OH)_2$ in brucite at T and P	–
x	initial $X_{Fe(OH)_2}$	–
y	parameter related to reaction progress as defined in Equation 2	–
r	hydrogen (H_2) production rate	mol s^{-1}
r_0	hydrogen production rate as defined in Equation S-3	mol s^{-1}
k_0	reaction kinetic constant of ferroan brucite alteration	mol m^{-2} s^{-1}
k_{ol}	reaction kinetic constant of olivine serpentinisation	mol m^{-2} s^{-1}
k_{MD}	maximum reaction constant provided in McCollom and Donaldson (2016) for H_2 production during olivine serpentinisation at 363 K	mol kg^{-1} s^{-1}
n_{H_2}	total amount of H_2 produced in the experiment	mol
$\bar{n}_{H_2}$	total amount of H_2 produced in the experiment normalised to the mass of starting Fe-brucite material	mol kg^{-1}
$n_{H_2,g}$	amount of H_2 in the gas phase	mol
$n_{H_2,eq}$	equilibrium amount of H_2 produced at T and P	mol
$n_{H_2,ol}$	amount of H_2 produced during Reaction S-8	mol
$n_{H_2,leak}$	amount of H_2 leaking in the model of serpentinised dunite alteration	mol
n_{ol}	amount of olivine in the serpentinised dunite in the model of serpentinised dunite alteration	mol
m_{water}	mass of water in contact with the rock at each time step of the serpentinised dunite alteration model	kg
m_{rock}	mass of rock in the serpentinised dunite alteration model	kg
λ	factor used to convert last measured n_{H_2} value into $n_{H_2,eq}$	–
$n°_{Fe}$, $n°_{Mg}$	initial number of moles of Fe and Mg in ferroan brucite	mol
A	ferroan brucite specific surface area	m^2 kg^{-1}
SA_{MD}	surface area of the olivine used in McCollom and Donaldson (2016)	m^2 kg^{-1}
SA	specific surface area of olivine calculated with the relationship provided in Brantley and Melott (2000) for a grain size of 500 µm, typical for serpentinised dunites in ophiolites (Malvoisin *et al.*, 2017)	m^2 kg^{-1}
R	universal gas constant	J mol^{-1} K^{-1}
T	temperature	K
Q_i	quotient of reaction i with i = 1 or 2	–
K_i	equilibrium constant of reaction i with i = 1 or 2	–
E_a	activation energy of reaction	J mol^{-1}
P_{H_2}	partial pressure of H_2 in the gas phase	bar
$P_{H_2,eq}$	partial pressure of H_2 in the gas phase at the equilibrium	bar
$[H_2]$	concentration of H_2 in the aqueous phase	mol m^{-3}
K_H	Henry's coefficient for H_2 gas	Pa m^3 mol^{-1}
V_g	volume of the gas phase	m^3
V_{aq}	volume of the aqueous phase	m^3
$\Delta_r G^{P,T}$	Gibbs free energy of reaction at T and P	J mol^{-1}
$\Delta_a H_i^{P,T}$	apparent enthalpy of phase i at T and P	J mol^{-1}
$S_i^{P,T}$	third-law entropy of phase i at T and P	J mol^{-1} K^{-1}
$\Delta_f H_i^\circ$	standard formation enthalpy of phase i (from the elements)	J mol^{-1}
$\Delta_f G_i^\circ$	standard formation Gibbs free energy of phase i	J mol^{-1}
S_i°	standard third-law entropy of phase i	J mol^{-1} K^{-1}
Cp_i	molar heat capacity function of phase i valid in the T_r–T temperature range	J mol^{-1} K^{-1}
V_i^0	molar volume of phase i at reference P_r and T_r	m^3 mol^{-1}
a_i	activity of phase i	–
ν_i	stoichiometric coefficient of phase i	–

Table S-1 continued.

Symbol	Definition	Units
T_r	reference temperature (298 K)	K
P_r	reference pressure (0.1 MPa)	Pa
T_j	temperature at equilibrium for experiment *j*	K
P_j	pressure at equilibrium for experiment *j*	Pa
f_j	sum of parameters which can be calculated from tabulated data of Klein *et al.* (2009) in Equation S-6	J mol^{-1} K^{-1}
J	constant fixing the H_2 escape rate in the model of serpentinised dunite alteration	kg s^{-1}
D	diffusion coefficient of H_2 in the fluid	m^2 s^{-1}
ρ_{water}	water density	kg m^{-3}
ρ_{rock}	rock density	kg m^{-3}
A_h	area of the horizontal section through which H_2 diffuses	m^2
h	vertical thickness of the serpentinised peridotite layer reacting in the model of serpentinised dunite alteration	m

Table S-2 Experimental conditions for each experiment, produced H_2 and XRD analysis results. Expected H_2 production assuming equilibrium is also calculated with PHREEQC using the thermochemical data retrieved in the present study. f-brc, ferroan brucite; mag, magnetite; pyr, pyroaurite; L/V, liquid-vapor equilibrium; n.d., not detected; n.c., not calculated; thermo., thermodynamic data used for determining thermodynamic parameters of $Fe(OH)_2$; and kin., kinetic data used for determining the kinetic law (predicted duration to reach measured n_{H_2} is not provided for these experiments). * 53.3 ± 16.5 wt. % Fe(III)-bearing brucite (see Carlin *et al.*, 2023) have also been detected in Run caps#t4. Errors are provided as ±3 times the standard deviation.

	Initial experimental conditions						XRD analysis output					PHREEQC	Kinetics	
run name	duration (h)	temperature (K)	initial pressure at T (MPa)	initial f-brc mass (g)	mass water-rock ratio	measured n_{H_2} from GC (mol)	$X_{Fe(OH)_2}$ in initial f-brc (%)	$X_{Fe(OH)_2}$ in final f-brc (%)	final f-brc (wt. %)	mag (wt. %)	pyr (wt. %)	simulated n_{H_2} at equilibrium (mol)	predicted duration to reach measured n_{H_2} (h)	use
caps#1	360	378	20	0.01-0.03	3.33-10	2.87E-09	15.6±2.1	11.0±1.2	93.8±1.2	3.2±0.6	3.3±0.9	1.80E-09	146	thermo.
caps#2	624	378	20	0.032	3.13	8.49E-09	15.6±2.1	12.9±1.8	95.3±1.2	4.7±1.2	n.d.	1.80E-09	267	thermo.
caps#3	984	423	20	0.046	2.17	2.11E-07	18.5±1.8	11.6±0.6	90.8±1.2	9.2±1.2	n.d.	3.07E-08	29	thermo.
caps#4	984	473	20	0.048	2.08	1.29E-06	18.5±1.8	15.8±0.3	92.8±0.6	7.2±0.6	n.d.	3.48E-07	1	thermo.
caps#6	1344	348	20	0.049	2.06	1.91E-10	17.9±2.1	14.7±1.5	89.2±2.1	6.3±1.2	4.5±1.8	5.50E-10	214	thermo.
caps#7	1344	403	20	0.049	2.06	1.91E-09	17.9±2.1	12.9±1.5	90.3±1.5	9.7±1.5	n.d.	1.00E-08	2	thermo.
caps#9	60	378	20	0.040	2.50	1.21E-07	18.1±2.7	13.7±2.1	99.8±0.3	0.2±0.3	n.d.	2.82E-09	2707	not used
caps#10	60	423	20	0.050	2.00	1.75E-07	18.1±2.7	10.2±2.4	97.4±0.9	2.6±0.9	n.d.	2.87E-08	23	thermo.
caps#11bis	60	473	20	0.050	2.00	5.88E-07	18.1±2.7	18.5±0.9	95.1±0.9	4.9±0.9	n.d.	3.27E-07	0.8	thermo.
caps#12bis	60	523	20	0.046	2.17	3.68E-06	18.1±2.7	16.2±0.9	92.6±0.9	8.4±0.9	n.d.	2.65E-06	<0.1	thermo.
caps#13	296	523	20	0.059	1.69	1.42E-06	18.1±2.7	19.8±0.3	92.0±0.9	8.0±0.9	n.d.	2.74E-06	<0.1	thermo.
caps#14	240	573	20	0.025	4.00	5.45E-06	18.1±2.7	12.1±0.6	83.6±1.2	16.4±1.2	n.d.	7.81E-06	<0.1	thermo.
caps#15	48	573	20	0.053	1.89	6.08E-06	18.1±2.7	15.6±0.6	87.3±1.2	12.7±1.2	n.d.	1.14E-05	<0.1	thermo.
SP#3	192	473	1.55 (L/V)	1.52	24.42	1.71E-04	15.6±2.1	20.1±0.3	94.0±0.9	6.0±0.9	n.d.	3.20E-04		kin./thermo.
SP#4	312	473	1.55 (L/V)	0.31	64.52	6.06E-05	18.5±1.8	16.0±0.6	90.7±0.6	9.3±0.6	n.d.	1.85E-04		kin./thermo.
SP#5	408	423	0.476 (L/V)	1.52	24.41	2.45E-05	17.9±2.1	17.7±0.9	93.4±0.9	6.6±0.9	n.d.	1.16E-04		kin./thermo.
SP#6	1656	378	5	1.495	19.80	4.89E-06	18.1±2.7	19.5±1.2	94.9±1.2	3.1±0.6	2.1±0.9	2.81E-05		kin./thermo.

Table S-2 continued.

	Initial experimental conditions						XRD analysis output					PHREEQC	Kinetics	
run name	duration (h)	temperature (K)	initial pressure at T (MPa)	initial f-brc mass (g)	mass water-rock ratio	measured n_{H_2} from GC (mol)	$X_{Fe(OH)_2}$ in initial f-brc (%)	$X_{Fe(OH)_2}$ in final f-brc (%)	final f-brc (wt. %)	mag (wt. %)	pyr (wt. %)	simulated n_{H_2} at equilibrium (mol)	predicted duration to reach measured n_{H_2} (h)	use
caps#t1	0.5	378	0.121 (L/V)	0.0624	1.60	8.13E-10	20.5±1.8	11.5±1.5	86.6±3	1.6±0.9	11.8±3	4.19E-07		not used
caps#t2	2	378	0.121 (L/V)	0.0639	1.56	5.58E-10	20.5±1.8	14.6±1.5	95.4±1.5	1.5±0.9	3.1±0.9	4.18E-07		not used
caps#t3	143	378	0.121 (L/V)	0.0656	1.52	1.53E-08	20.5±1.8	13.5±1.2	84.8±2.4	2.8±0.9	12.4±2.4	4.17E-07		not used
caps#t4	335	378	0.121 (L/V)	0.0567	1.76	4.62E-10	20.5±1.8	n.c.	39.4±2.1*	3.1±0.9*	18.0±3.9*	4.23E-07		not used
caps#t5	0.5	423	0.476 (L/V)	0.0421	2.38	7.33E-10	20.5±1.8	13.7±1.5	90.2±2.4	1.8±0.9	8.1±2.4	2.65E-06		kin.
caps#t6	72	423	0.476 (L/V)	0.027	3.71	8.79E-09	20.5±1.8	14.6±0.9	98.2±0.6	1.8±0.6	n.d.	2.53E-06		kin.
caps#t7	163	423	0.476 (L/V)	0.0509	1.97	4.93E-08	20.5±1.8	15.4±0.9	97.9±0.6	2.1± 0.6	n.d.	2.67E-06		kin.
caps#t8	483	423	0.476 (L/V)	0.0519	1.93	2.02E-07	20.5±1.8	15.0±0.9	97.6±0.6	2.4±0.6	n.d.	2.67E-06		kin.
caps#t9	721	423	0.476 (L/V)	0.0527	1.90	5.57E-07	20.5±1.8	15.8±0.9	96.9±0.6	3.1±0.6	n.d.	2.68E-06		kin.
caps#t11	1872	423	0.476 (L/V)	0.0557	1.80	1.38E-06	20.5±1.8	20.8±0.3	95.6±0.6	4.4±0.6	n.d.	2.69E-06		kin.
caps#t12	3552	423	0.476 (L/V)	0.0454	2.20	2.33E-06	20.5±1.8	19.7±0.3	94.1±0.9	6.0±0.9	n.d.	2.63E-06		kin./thermo.

Table S-3 Evolution of the number of moles of H_2 (n_{H_2}) measured with gas chromatography as a function of time for SP#6 (378 K, 5 MPa).

duration (h)	measured n_{H_2} from GC (mol)
0	1.12E-07
5	1.44E-07
22	1.80E-07
51	2.31E-07
77	2.53E-07
150	3.24E-07
188	3.63E-07
219	3.41E-07
312	5.17E-07
363	5.22E-07
744	2.76E-06
987	3.55E-06
1078	4.00E-06
1198	4.42E-06
1323	4.58E-06
1390	4.73E-06
1487	4.70E-06

Table S-4 Summary of available $Fe(OH)_2$ thermodynamic data. *a*, *b* and *c* are the coefficients of the equation of Maier and Kelley (1932) for C_p: $C_p = a + bT + cT^{-2}$.

References	$\Delta_f H^\circ$	$\Delta_f G^\circ$	S°	*a*	*b*	*c*
	kJ/mol	kJ/mol	J/mol/K	J/mol/K	(10^3) J/mol/K^2	(10^{-5}) J K/mol
Wagman *et al.* (1982) - NBS	-569.0	-486.5	88.0			
Chase (1998) - NIST-JANAF	-574.045	-491.97	87.864	97.069		
Leussing and Kolthoff (1953)		-492.58				
Refait *et al.* (1999)		-490				
Ziemniak *et al.* (1995)	-583.39	-500.16	84	90		
Sverjensky and Molling (1992)		-494.97				
McCollom and Bach (2009)	-574.61*	-492.58†	88.0‡	109.035	18.192	-22.51
This study	-581.3*	-498.90	86.4	109.035**	18.192**	-22.51**

*: computed from $\Delta_f G^\circ = \Delta_f H^\circ - 298.15\Delta_f S^\circ$ with the values of $\Delta_f H^\circ$ and S° provided in the table and standard entropies of the elements taken from Helgeson *et al.* (1978).
†: taken from Leussing and Kolthoff (1953).
‡: taken from Wagman *et al.* (1982).
**: taken from McCollom and Bach (2009), calculated as a linear function of brucite, greenalite and chrysotile C_p functions.

Supplementary Figures

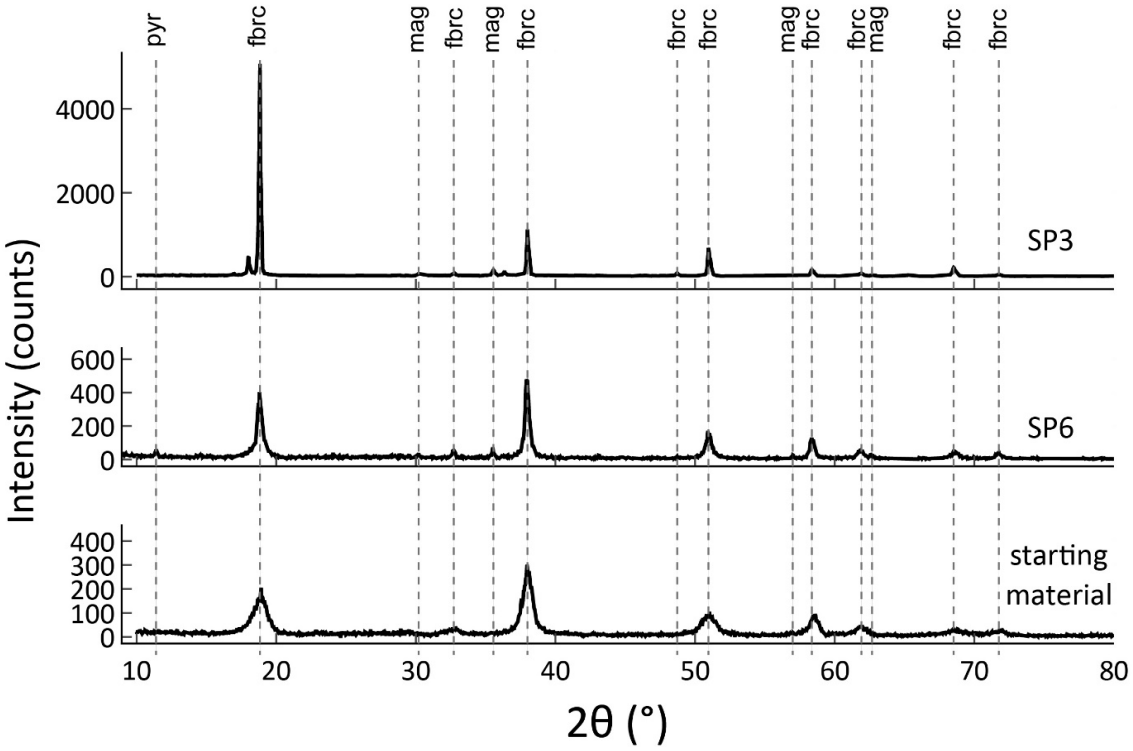

Figure S-1 Selected XRD patterns. From bottom to top: synthetic ferroan brucite starting material, Run SP#6 (378 K, 69 days) and Run SP#3 (473 K, 8 days). fbrc, ferroan brucite; mag, magnetite; pyr, pyroaurite. CuKα radiation.

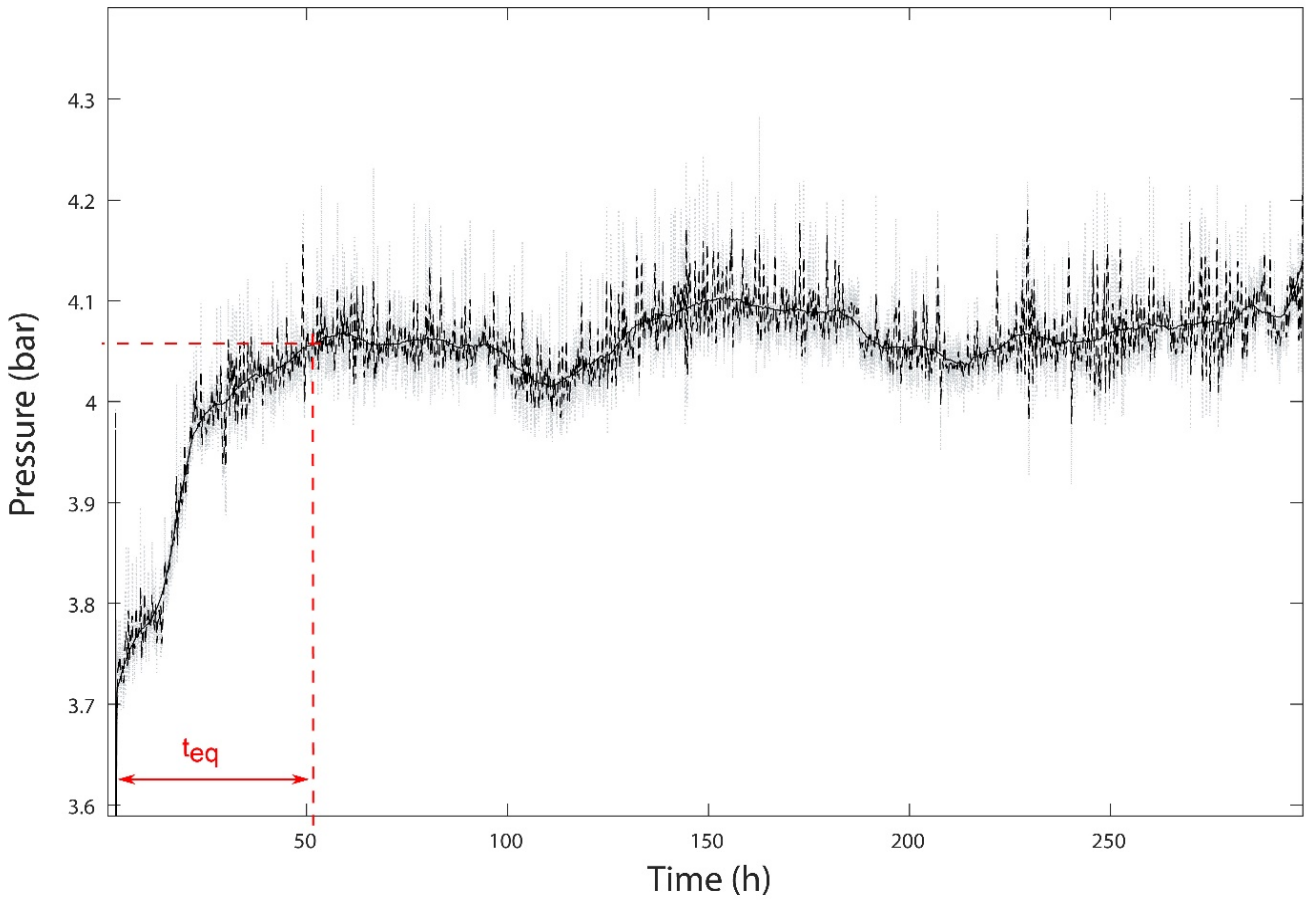

Figure S-2 *In situ* pressure monitoring for SP#5. The grey dotted line, the black dashed line and the solid black curve correspond, respectively, to the raw pressure data, the pressure filtered with a low pass filter, and smoothed filtered pressure. The time to reach equilibrium (t_{eq}; red dashed lines) is graphically determined.

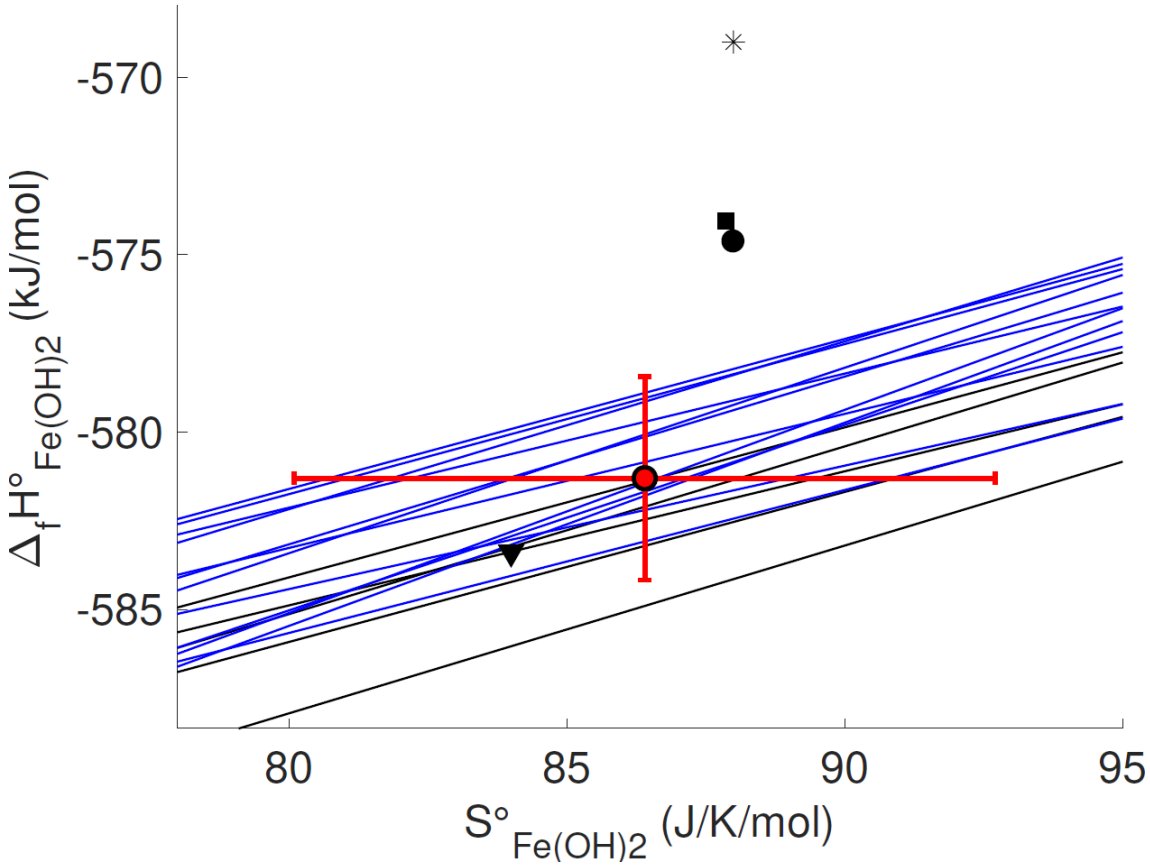

Figure S-3 $\Delta_f H°_{Fe(OH)2}$ *vs.* $S°_{Fe(OH)2}$ relationship determined for capsules experiments (blue lines) and titanium reactor experiments (black lines). The best-fitting $\Delta_f H°_{Fe(OH)2}$ and $S°_{Fe(OH)2}$ values ± their standard error determined by linear regression (R^2 = 0.926) are displayed with a red dot. The black circle, square, triangle and star correspond to the thermodynamic data of McCollom and Bach (2009), Chase (1998), Ziemniak *et al.* (1995) and Wagman *et al.* (1982), respectively.

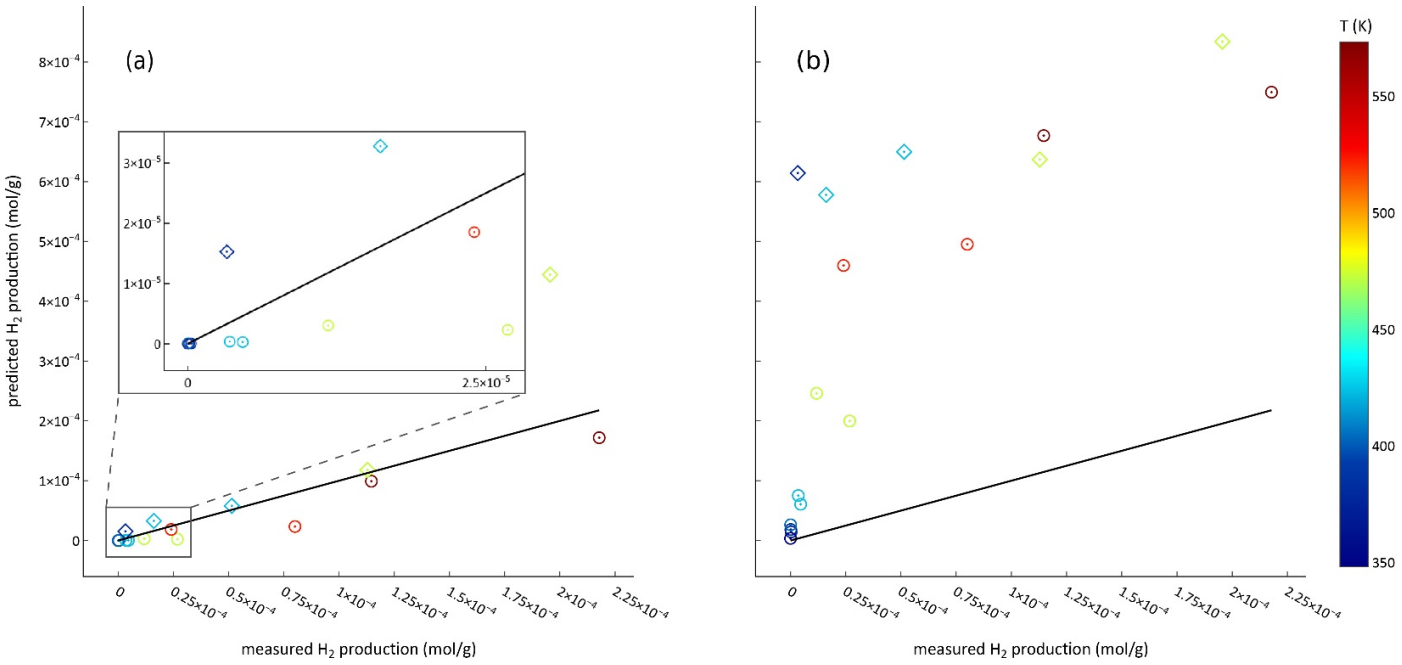

Figure S-4 Measured *vs*. predicted moles of H_2 produced per gram of ferroan brucite in experiments SP#3 to #6 and caps#t12 (diamond symbols), and caps#1 to #15 (circle symbols). The predicted amount of H_2 is equal to the measured amount of H_2 on the black solid line. The predictions were calculated with PHREEQC using the thermodynamic data for $Fe(OH)_2$ **(a)** derived here and **(b)** from Klein *et al.* (2009).

Supplementary Information References

Brantley, S.L., Mellott, N.P. (2000) Surface area and porosity of primary silicate minerals. *American Mineralogist* 85, 1767–1783. https://doi.org/10.2138/am-2000-11-1220

Carlin, W., Malvoisin, B., Lanson, B., Brunet, F., Findling, N., Lanson, M., Magnin, V., Fargetton, T., Jeannin, L., Lhote, O. (2023) Fe^{III}-substituted brucite: Hydrothermal synthesis from $(Mg_{0.8}Fe^{II}_{0.2})$-brucite, crystal chemistry and relevance to the alteration of ultramafic rocks. *Applied Clay Science* 234, 106845. https://doi.org/10.1016/j.clay.2023.106845

Chase, M.W. (1998) *NIST-JANAF Thermochemical Tables*. Fourth Edition, American Chemical Society, Washington, DC.

Doebelin, N., Kleeberg, R. (2015) *Profex*: a graphical user interface for the Rietveld refinement program *BGMN*. *Journal of Applied Crystallography* 48, 1573–1580. https://doi.org/10.1107/S1600576715014685

Helgeson, H.C., Delany, J.M., Nesbitt, H.W., Bird, D.K. (1978) Summary and critique of the thermodynamic properties of rock-forming minerals. *American Journal of Science* 278-A, 1–229.

Klein, F., Bach, W., Jöns, N., McCollom, T., Moskowitz, B., Berquó, T. (2009) Iron partitioning and hydrogen generation during serpentinization of abyssal peridotites from 15°N on the Mid-Atlantic Ridge. *Geochimica et Cosmochimica Acta* 73, 6868–6893. https://doi.org/10.1016/j.gca.2009.08.021

Lasaga, A.C. (1998) *Kinetic Theory in the Earth Sciences.* Princeton University Press, Princeton, NJ.

Leussing, D.L., Kolthoff, I.M. (1953) The Solubility Product of Ferrous Hydroxide and the Ionization of the Aquo-Ferrous Ion. *Journal of the American Chemical Society* 75, 2476–2479. https://doi.org/10.1021/ja01106a058

Maier, C.G., Kelley, K.K. (1932) An Equation for the Representation of High-Temperature Heat Content Data. *Journal of the American Chemical Society* 54, 3243–3246. https://doi.org/10.1021/ja01347a029

Malvoisin, B., Brunet, F., Carlut, J., Montes-Hernandez, G., Findling, N., Lanson, M., Vidal, O., Bottero, J.-Y., Goffé, B. (2013) High-purity hydrogen gas from the reaction between BOF steel slag and water in the 473–673 K range. *International Journal of Hydrogen Energy* 38, 7382–7393. https://doi.org/10.1016/j.ijhydene.2013.03.163

Malvoisin, B., Brantut, N., Kaczmarek, M.-A. (2017) Control of serpentinisation rate by reaction-induced cracking. *Earth and Planetary Science Letters* 476, 143–152. https://doi.org/10.1016/j.epsl.2017.07.042

McCollom, T.M., Bach, W. (2009) Thermodynamic constraints on hydrogen generation during serpentinization of ultramafic rocks. *Geochimica et Cosmochimica Acta* 73, 856–875. https://doi.org/10.1016/j.gca.2008.10.032

McCollom, T.M., Donaldson, C. (2016) Generation of Hydrogen and Methane during Experimental Low-Temperature Reaction of Ultramafic Rocks with Water. *Astrobiology* 16, 389–406. https://doi.org/10.1089/ast.2015.1382

Refait, Ph., Bon, C., Simon, L., Bourrié, G., Trolard, F., Bessière, J., Gènin, J.-M.R. (1999) Chemical composition and Gibbs standard free energy of formation of Fe(II)-Fe(III) hydroxysulphate green rust and Fe(II) hydroxide. *Clay Minerals* 34, 499–510. https://doi.org/10.1180/000985599546280

Sverjensky, D.A., Molling, P.A. (1992) A linear free energy relationship for crystalline solids and aqueous ions. *Nature* 356, 231–234. https://doi.org/10.1038/356231a0

Wagman, D.D., Evans, W.H., Parker, V.B., Schumm, R.H., Halow, I., Bailey, S.M., Chruney, K.L., Nuttall, R.L. (1982) The NBS tables of chemical thermodynamic properties: Selected values for inorganic and C_1 and C_2 organic substances and SI units. *Journal of Physical and Chemical Reference Data* 11, Suppl. 2, 1–392. https://srd.nist.gov/JPCRD/jpcrdS2Vol11.pdf

Ziemniak, S.E., Jones, M.E., Combs, K.E.S. (1995) Magnetite solubility and phase stability in alkaline media at elevated temperatures. *Journal of Solution Chemistry* 24, 837–877. https://doi.org/10.1007/BF00973442